Original Article

Young's modulus and hardness of multiphase CaZrO$_3$-MgO ceramics by micro and nanoindentation

Abílio P. Silva[a,b], Fernando Booth[a,c], Liliana Garrido[c], Esteban Aglietti[c], Pilar Pena[a], Carmen Baudín[a,*]

[a] Instituto de Cerámica y Vidrio, ICV-CSIC, Kelsen 5, Madrid 28049, Spain
[b] Centre for Mechanical and Aerospace Science and Technologies (C-MAST-UBI), Universidade da Beira Interior, Rua Marquês d'Ávila e Bolama, 6201-001, Covilhã, Portugal
[c] CETMIC (Centro de Tecnología de Recursos Minerales y Cerámica, CIC-CONICET La Plata), Camino Centenario y 506, C.C.49 (B1897ZCA) M.B. Gonnet, Buenos Aires, Argentina

A R T I C L E   I N F O

A B S T R A C T

The aim of this work is to determine the values of the hardness and elastic modulus of the phases present in CaZrO$_3$-MgO-ZrO$_2$ composites and to analyse their contribution to the composite properties. Two materials previously developed with the same major phases (CaZrO$_3$, MgO and c-ZrO$_2$) present in different volume fractions and grain size have been analysed. The hardness and Young's modulus of each phase determined by nanoindentation are independent from the specific composite and coincident with nanoindentation values for single phase bulk materials. The contribution of the individual phases to Young's modulus of the multiphase materials is in agreement with calculations using the nanoindentation values and the Voight upper limit of the "rule of mixtures". Scale effect due to microcracking has been observed for micro-hardness values of the composites and differences between calculations and experimental values are related to this effect.

1. Introduction

The recent trends in materials engineering favour composite materials as opposed to single phase ones. In this sense, considerable improvement in the properties of ceramics has been attained by combining one or more components to obtain ceramic–ceramic composites.

As examples, in the field of advanced ceramics for severe conditions of service, composite materials are widely used as cutting tools [1] and are under development for thermal and environmental barrier coatings (TBC, EBC) [2,3], due to their excellent thermal and chemical stability together with high wear resistance.

However, the most known multiphase ceramics for severe environments are refractories. This ceramic family is responsible for the success of essential industries connected to high temperature processing, such as glass factories, cements, thermoelectric power stations and foundries [4,5].

In particular, oxide refractories such as those based on mullite, corundum or zirconia with compositions in ternary multiphase systems Al$_2$O$_3$-SiO$_2$-XO (X = Mg, Ca), Al$_2$O$_3$-SiO$_2$-ZrO$_2$, Al$_2$O$_3$-CaO-MgO and ZrO$_2$-CaO-MgO are traditional examples [4–9]. Additionally, more complex compositions in the quaternary systems Al$_2$O$_3$-SiO$_2$-MgO-CaO or Al$_2$O$_3$-SiO$_2$-MgO-ZrO$_2$ are also usual [7].

The successful design of multiphase ceramics requires an integrated approach which takes into account the equilibrium phase constitution and how the properties of the constituent phases affect the global behaviour of the material.

This work is a part of a wider project focused to the development of new multiphase oxide ceramics for structural applications of high responsibility with compositions inspired by those of refractories. The ternary system ZrO$_2$-MgO-CaO has been chosen due to the high temperature of its eutectic point, 1982 °C [8,9]. Two fine grained and dense ZrO$_2$-CaZrO$_3$-MgO materials with sufficient strength and excellent wear resistance in sliding contact against steel and zirconia have been developed [10–12]. Further compositional designs focusing the improvement of the mechanical behaviour would require a detailed knowledge of properties of the constituent phases and how they affect the overall behaviour of the materials.

In principle, the macroscopic properties of multiphase ceramics would depend on the properties of the individual constituent phases and their distribution in the microstructure – volume fraction, particle size, shape, orientation and location – together with the characteristics of the grain boundaries and the porosity. In addition, the final

* Corresponding author.
  E-mail address: cbaudin@icv.csic.es (C. Baudín).

properties might also depend on residual stresses developed during cooling from the sintering temperature due to thermal expansion mismatch of individual grains.

Micromechanical models aim at predicting the effective macroscopic properties of heterogeneous materials from the knowledge of the characteristics of their various microstructural components. In this sense, the determination of the intrinsic properties of each phase separately in multiphase materials is needed for the development of new materials with focused properties.

Several macroscopically homogeneous and isotropic composites comprise material phases that cannot be recapitulated *ex situ*, most studied examples of such phases are calcium silicate hydrates in cementitous materials (see [13] for a review) and hydroxyapatite in bone (e.g. [14]). In the same way, heterogeneous anisotropic composites such as layered or coated materials present a similar problem, being the thin films a clear example of this behaviour [15]. Moreover, even for phases whose properties can be determined in bulk specimens, their characteristics when included in a composite are often somewhat different from material characteristics in bulk pieces [16–18]. Thus, in many cases the mechanical characterization of the constituent phases, in order to deduce their contribution to the overall behaviour of the composite, obviates conventional mechanical testing of large representative specimens.

The evaluation of the *in situ* elastic properties and hardness of the constituent phases of composites involves measurements at small volumes, which, in principle, can be accomplished by instrumented nanoindentation tests. The local properties of materials are determined by monitoring the penetration depth of an indenter tip of definite geometry as a function of applied load. Young's modulus and hardness are calculated from the contact stiffness, i.e. the slope of the initial portion of the unloading curve, employing the Oliver-Pharr method [19]. Extensive work has been dedicated to extract the local mechanical characteristics of ceramics from the loading-unloading curves [13–18,20–27].

Initially, the method was applied to characterise thin films of known thickness. In some cases, the thin film properties are extrapolated for indentation depth approaching zero (e.g. [23]). Another method consists in using the ratio Load/Stiffness to determine the range of indentation depth where the effects of the substrate are minimized (e.g.

[24]).

In order to characterize multiphase bulk materials, the grid indentation statistical analysis was proposed by Ulm et al. [20] and has successfully been applied to assess mean properties of separate phases in different ceramic materials [13–17,21,22]. The method involves the analysis of a large number of indentations performed blindly on the surface assuming that the frequency of results is determined by the volume fraction of the phases. This method is especially useful for materials in which the particles of the constituent phases are difficult to identify by microscopy and have similar mechanical behaviour.

In materials with constituents of different nature resulting in different responses to loading in terms of elastic-plastic behaviour, the characteristics of the curves might serve as a guide to differentiate the indented phases [15,18].

When the phases present in the material can be identified by microscopic means, it is not necessary to realise deconvolution and statistical analysis. In some cases, it is possible to identify the phase prior to performing the indentations [25]. Alternatively, blind indentation grids can be done and the residual imprints can be associated to the recorded load-displacement curves after testing by microscopy [22,25–27].

The aim of this work is to determine the values of the hardness and elastic modulus of the phases present in $CaZrO_3$-MgO-ZrO_2 composites and to analyse the contribution of each phase to the hardness and elastic modulus of the materials.

Two materials previously developed [10–12], with the same major phases ($CaZrO_3$, MgO and c-ZrO_2) but in different volume fractions and grain size have been analysed. The hardness and Young's modulus of each phase have been determined by nanoindentation and compared to those of bulk materials. The expected contribution of the phases to the properties of the composite has been evaluated by means of simple models and compared to the properties of the multiphase ceramics.

A summary of values reported in the literature for $CaZrO_3$, MgO and c-ZrO_2 bulk materials is presented in Table 1 [26,28–38]. Only macroscopic data have been found for $CaZrO_3$, for which Vickers indentation values between 8 and 11 GPa and Young's modulus around 230 GPa have been reported. Nanoindentation has been used to characterise single crystals of MgO; reported Young's modulus values (≈ 280–290 GPa) are in the same range as bulk values calculated for

Table 1
Mechanical properties for bulk specimens of the major phases present in the studied materials.

	density		E (GPa)	H (GPa)	Materials	Methods	Ref.
	TD (%)	ρ (g/cm³)					
$CaZrO_3$	97			9.20 ± 0.17	$CaO:ZrO_2 = 51:49$ mol%	HV	28,29
				10.61 ± 0.11	$CaO:ZrO_2 = 45:55$ mol%		
	97–98			8.42 ± 0.11	Stoichiometric grain size: 1–4 μm		
			≈230	11		HV	30
	96.8	4.46	224 ± 1	8.1 ± 0.1	Polycrystalline bulk samples prepared by SPS	ultrasonic pulse-echo; HV (9.8 N, 15 s)	31
	95–96		~231		grain size < 5 μm	pulse-echo	32
MgO	≈99	3.5	≈270			3 point bending	33
	100		≈278[*]				
			274 ± 15.2[**]	9.95 ± 0.3	single crystal	Nanoindentation (500–1500 μN)	34
			290 ± 38	8.4 ± 1.7	single crystal	Nanoindentation (50–200 nm, 25–400 mN)	35
				9.19	single crystal	Nanoindentation h > 400 nm	36
			≈12			h < 200 nm	
c-ZrO_2			248	19.8	9.5 mol% Y, single crystal	Nanoindentation (1–650 mN, 20–1000 nm)	26
			250	19.5	2.8 mol% Y, grain size 3.84–4.63 μm, duplex[***] (cubic) microstructure		
	96.9		210.2 ± 5.2[**]	16.2 ± 0.6	8 mol% Y, grain size 3.43 μm	Nanoindentation (5 mN, 1 mN/s, hold 2 s)	37
	100		≈231[*]	≈17.8[*]			
			240 ± 9	19.6 ± 0.7	Industrial Ca-stabilised zirconia	Nanoindentation (6 mN, 0.6 mN/s, hold 10 s)	[****]

* Calculated for zero porosity using [38].
** Calculated from Er = 187.5 ± 5.2 using E_i = 1141 GPa and Poisson's ratio of 0.07.
*** Duplex material (cubic and tetragonal) zirconia.
**** Industrial Ca-stabilised zirconia characterised in this work.

zero porosity materials from bending data. Hardness of the single crystals has been found to decrease with increasing indentation depth. It has not been possible to find data for Ca-stabilised ZrO_2. Young's modulus and hardness determined by nanoindentation on a YSZ single crystal and cubic grains in YSZ duplex materials are similar ($E \approx 250$ GPa, $H \approx 20$ GPa) while single phase materials with 8 mol% of Y_2O_3 present slightly lower values ($E \approx 230$ GPa, $H \approx 18$ GPa).

2. Experimental

The complete characterisation of the raw materials and the detailed processing procedure to fabricate fine grained and dense $CaZrO_3$-MgO-ZrO_2 multiphase ceramics are reported elsewhere [10]. The starting materials were two different natural dolomites ($MgCa(CO_3)_2$) from Argentina and high purity ZrO_2 (Saint Gobain – Zir Pro, China). The designation of the materials was DBZ for the equimolar mixture of m-ZrO_2 and the purest dolomite (CaO + MgO = 97.4 wt.% and $SiO_2 < 2$ wt.%) and DNZ for the equimolar mixture of m-ZrO_2 and the low purity dolomite (CaO + MgO = 86.5 wt.% and SiO_2 = 10.2 wt.%). Attrition milled powder mixtures were uniaxially pressed and sintered at 1450 °C during 2 h to reach discs specimens of 10 mm diameter and 8 mm thickness. Testing surfaces were polished using diamond paste down to 3 μm. Three nominally identical specimens were used for characterising each material.

Vickers hardness (Mitutoyo AVK-C2) was performed with load of 100 N during 15 s following the procedure described in ASTM C 1327. Five valid indentations were used for each material.

Nanoindentation tests were conducted at room temperature in air, using a Nano NH-3 (CETR, USA) with an atomic force microscope (AFM), which has load and depth sensing resolutions of 0.03 μN and 0.02 nm, respectively. A Berkovich diamond indenter of 100 nm tip radius was used to perform indentations during 10 s with loading and unloading rates of 0.05 mm/s. Curves of applied indentation load (P) as a function of penetration depth (h) were recorded during both loading and unloading. From these curves, hardness (H) and Young's modulus (E) were calculated employing the model proposed by Oliver and Pharr [19].

The recorded data were corrected for the elastic recovery determined considering the unloading residual depth with less than 10% of maximum load applied. The contact area and the frame stiffness were calibrated using fused silica.

Nine matrices of 3 × 3 indents (span of 20 μm) were performed in each material attempting to determine the bulk (composite) and local (individual phase) responses. Each matrix consisted in one large indentation (load = 500 mN; penetration depth ∼1600 nm; loading rate ∼50 mN/s) and eight small ones (load = 6 mN; penetration depth ∼160 nm; loading rate ∼0.6 mN/s), with holding of 10 s at maximum load. Reported values for the results obtained from the large Berkovich indentations (nine in each material) are the average of at least six results and errors are the standard deviations.

All residual imprints were inspected using a field emission scanning electron microscope equipped with an energy dispersive X-ray spectroscopy (EDX) system (FE-SEM, Hitachi, S-4700, type I, Japan). In this way, it was possible to identify whether the indentations were valid –i.e. performed inside the grains- or they were located at grain boundaries or pores. Moreover, it was possible to identify the specific phase in which the valid indentations were embedded. The number of valid determinations for each phase is described in the results.

In addition, an industrial specimen of Ca-stabilised zirconia was tested by nanoindentation under the same conditions and the marks located in dense areas where identified and used for calculations.

3. Results

The complete microstructural characteristics of the studied materials (DBZ, DNZ) are reported elsewhere [10]. Both materials were dense ($\approx 100\%$ and $97 \pm 1\%$ of theoretical density for DBZ and DNZ, respectively) and homogeneous.

Regarding the crystalline constituents, major phases in DBZ were $CaZrO_3$ (75.4 ± 0.5 wt.%) and MgO (18.8 ± 0.4 wt.%); c-ZrO_2 ($Ca_{0.15}Zr_{0.85}O_{1.85}$, 2.2 ± 0.1 wt.%) and merwinite ($Ca_3Mg(SiO_4)_2$, 3.7 ± 0.3 wt.%) were present as minor phases. The main crystalline phases in DNZ were $CaZrO_3$ (54.0 ± 0.9 wt.%), c-ZrO_2 ($Ca_{0.15}Zr_{0.85}O_{1.85}$, 17.5 ± 0.5 wt.%), MgO (16.2 ± 0.5 wt.%) and merwinite ($Ca_3Mg(SiO_4)_2$, 11.5 ± 1.2 wt.%); Ca_2SiO_4 was present in a low amount (0.66 ± 0.3 wt.%) as minor phase. As it will be observed in the figures, major phases presented distinct colours when analysed by FE-SEM: MgO was dark gray, calcium zirconate was light gray and zirconia was brilliant white. 4 and 10 wt.% of non-diffracting phases were also identified by Rietveld analysis in DBZ and DNZ, respectively. Dark areas of variable composition observed by FE-SEM, especially in DNZ, would correspond to these non-diffracting phases and/or merwinite.

A characteristic AFM image of the 3 × 3 nanoindentation matrices performed in the multiphase materials shown in Fig. 1a. This image helped to localise the different indentations in order to identify their location in the microstructure by FE-SEM (Fig. 1b). Similar procedure was performed for Ca-stabilised zirconia (Fig. 1c). The industrial specimen was relatively porous so only nanoindentations in dense portions of the material could be used to determine the reference values for Ca-stabilised ZrO_2 shown in Table 1. The obtained values are similar to those reported by Gaillard et al. [26] for single crystals and individual cubic grains of YSZ.

Fig. 2 shows characteristic Vickers indentations for both multiphase materials. The imprints affect large material volumes constituted by numerous grains of the different phases. Cracks emerging from the vertices of both imprints are observed. Some cracks are observed at the edges of the imprints, especially in DNZ in which the edges are heavily cracked and numerous grains have been detached from them (Fig. 2b). The constituent phases are easily distinguishable by the colours. DBZ material has $CaZrO_3$ grains (light gray) with sizes, $\varphi \approx 2$–6 μm, MgO grains (dark gray) with $\varphi \approx 3$ μm, and c-ZrO_2 grains (brilliant white) with $\varphi \approx 2.5$ μm. Microstructure of DNZ is coarser, with $CaZrO_3$ and MgO grains with $\varphi \approx 2$–15 μm and 1–4 μm, respectively. c-ZrO_2 grains in DNZ, with $\varphi \approx 1$–2 μm, are smaller than in DBZ.

Fig. 3 shows results of the large Berkovich indentations for both materials and the corresponding load-penetration curves. Several grains of the different phases are embedded in the imprint for material DBZ (Fig. 3a) while the large grains of DNZ (Fig. 3b) are only partially embedded in the imprint. In both materials, cracks emerge from the vertices but no detachment of grains is observed. There are no discontinuities in the load-depth curve of DBZ while an increase in depth for constant load during the holding period at maximum load was detectable in the curves of DNZ (Fig. 3c). Such feature is usually called "pop-in".

Table 2 summarizes the bulk properties of the materials calculated using the high load Vickers and Berkovich indentations. Young's modulus for DNZ is slightly lower than for DBZ. Vickers indentation gives lower values of hardness for DNZ than for DBZ while the high variability associated to Berkovich hardness values of DNZ impedes to detect the potential differences between the materials.

Using FE-SEM it was possible to localise a total of 62 and 60 imprints in DBZ and DNZ specimens, respectively.

In DBZ 45 imprints were embedded in well differentiated phases − 37, 3 and 5 in $CaZrO_3$, c-ZrO_2, MgO, respectively- and 35 in DNZ specimens − 21, 8 and 6 in $CaZrO_3$, c-ZrO_2, and MgO, respectively. Fig. 4 shows representative imprints localised in c-ZrO_2, $CaZrO_3$, and MgO grains and Fig. 5 shows the corresponding load (P) versus depth (h) curves. Imprints shown in Fig. 4 are small enough to be completely embedded in the grains. None of the imprints presented the characteristic shape of significant pile-up or sink-in [40] and the P-h curves did not exhibit any sign of discontinuity that would reveal fracture-like
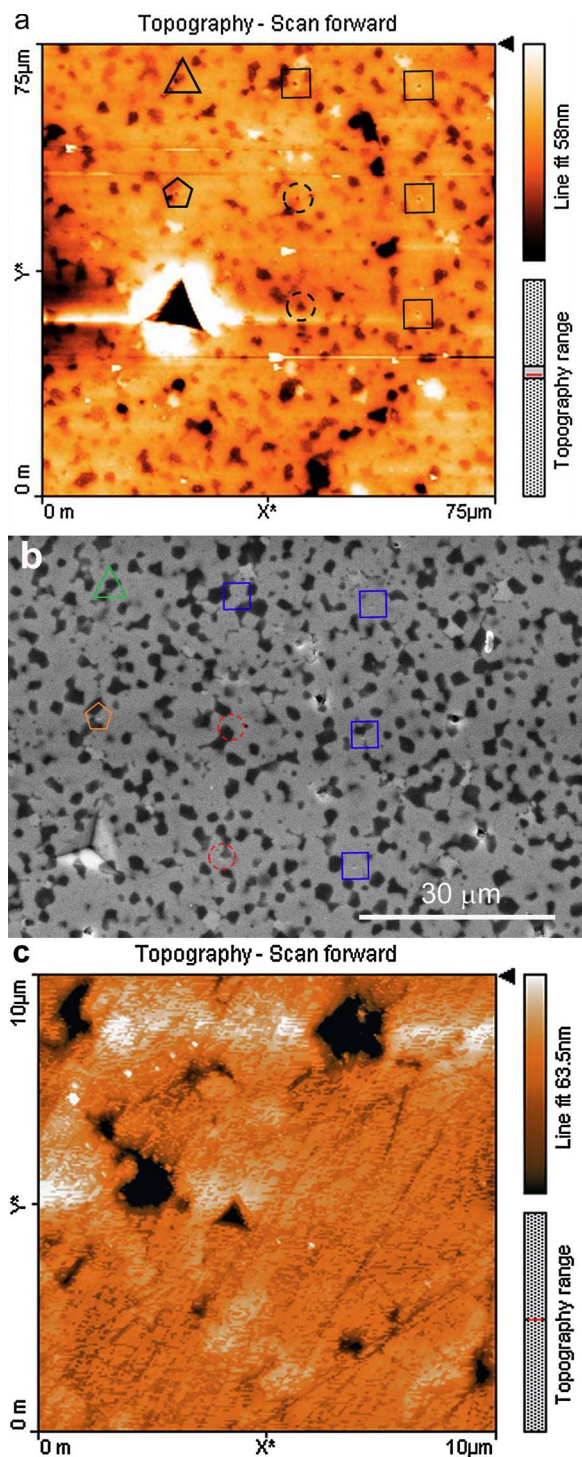
Fig. 1. Example of the procedure used to identify the indentations in the microstructure of the materials. Matrix of 3 × 3 Berkovich indentations (span of 20 μm) on the surface of a DBZ specimen.

a) AFM image where a large imprint (edge of ~10 μm) and eight nanoindentations (edge of ~600 nm) are observed.

b) FE-SEM image where the location of the imprints of figure (a) in the microstructure can be identified. Circles, squares, triangles and pentagons correspond to indentations located at grain boundaries, $CaZrO_3$ grains, MgO grains, and c-ZrO_2 grains, respectively.

c) AFM image of the industrial Ca-stabilised zirconia where a nanoindentation (edge of ~600 nm) is observed.

phenomena, therefore, they were used to obtain the local hardness and Young's modulus of c-ZrO_2, $CaZrO_3$, and MgO plotted in Fig. 6.

17 and 16 imprints were found in grain boundaries of DBZ and DNZ

specimens, respectively. Additionally, 9 imprints were observed in black areas of DNZ specimens. As discussed elsewhere [10] these areas are relatively small and with highly variable chemical composition and shape, thus, it is not possible to discern their nature. Moreover, the associated ranges of E and H values were extremely broad.

4. Discussion

The features of the residual imprints corresponding to Vickers indentations, with cracks along the edges and grains detached are typical of polycrystalline ceramics presenting residual stresses (e.g. alumina [41]). In these materials microcracks develop under the highly localized loads involved in indentation testing, depending on the grain size and the relative orientation of the grains.

The materials studied here are prone to the development of residual stresses during cooling from the sintering temperature due to thermal expansion mismatch between the different phases present α average between 298 and 1675 K, $\alpha \approx 10 \times 10^{-6}\,K^{-1}$ for $CaZrO_3$ [42] and c-ZrO_2 stabilised with Yttria [43] and $\alpha \approx 12 \times 10^{-6}\,K^{-1}$ for MgO [44] and, especially, due to the crystalline thermal expansion anisotropy of $CaZrO_3$ ($\alpha_c = 4.9 \times 10^{-6}\,K^{-1}$, $\alpha_b = 10.9 \times 10^{-6}\,K^{-1}$, $\alpha_c = 15.1 \times 10^{-6}\,K^{-1}$ [42]). Therefore, cracks develop under the Vickers indenter especially in materials DNZ, which presents much larger grain sizes (Fig. 2b).

For DBZ, there are no significant differences between Vickers and Berkovich bulk hardness values because both kinds of imprints affect material volumes representative of the microstructure (Figs. 2 and 3 a). The large grains in DNZ were only partially embedded in the Berkovich
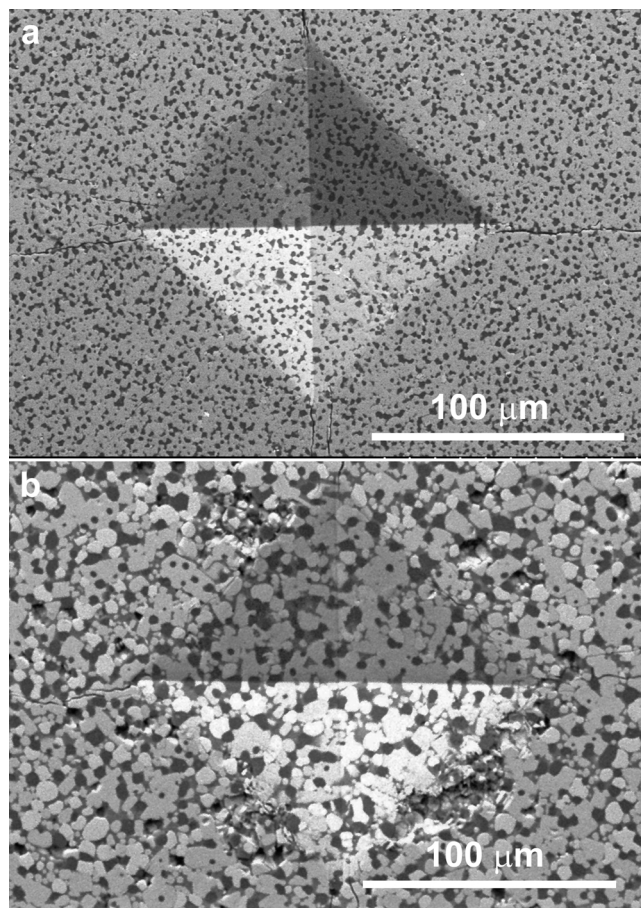

Fig. 2. Characteristic Vickers indentations (100 N, 15 s) observed by FE-SEM. Cracks emerging from the vertices are observed.

a) Material DBZ. Cracks are observed along the edges.

b) Material DNZ. Grain detachment and cracks are observed along the edges.

Table 2
Bulk mechanical properties of the studied multiphase materials, DBZ and DNZ.

Material	Vickers		Berkovich		Calculated[**]	
	HV (GPa)	H (GPa)[*]	H (GPa)	E (GPa)	H (GPa)	E (GPa)
DBZ	8.8 ± 0.4	9.5 ± 0.4	10 ± 1	220 ± 10	12.3 ± 0.9	227 ± 12
DNZ	7.5 ± 0.4	8.1 ± 0.4	9 ± 3	199 ± 29	12.0 ± 0.7	205 ± 10

* Calculated using H = 1.0785HV [39].

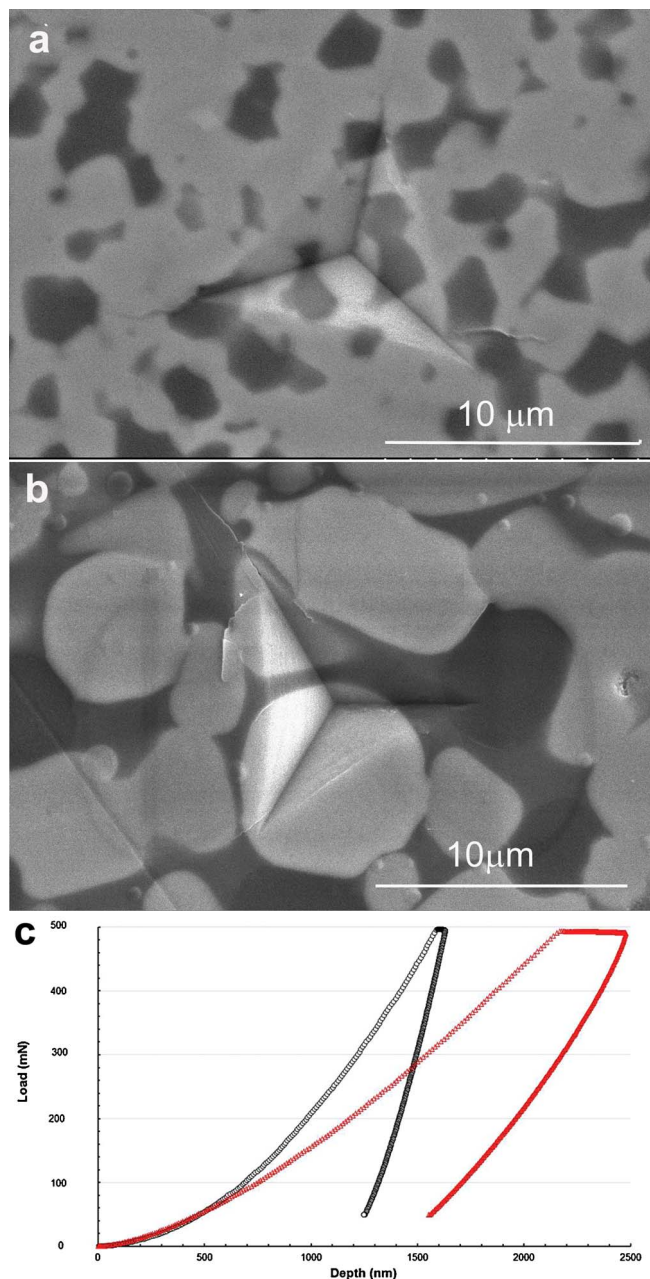** Using data from Table 4.

Fig. 3. Results from Berkovich indentation at high load (500 mN, 10 s).
a) Characteristic residual imprint in DBZ embedding a representative portion of the microstructure. FE-SEM micrograph. Cracks emerging from the vertices are observed.
b) Residual imprint in DNZ with grains partially embedded. FE-SEM micrograph. Cracks emerging from the vertices are observed.
c) Load (P) versus depth (h) curves corresponding from Berkovich indentations at 500 mN.
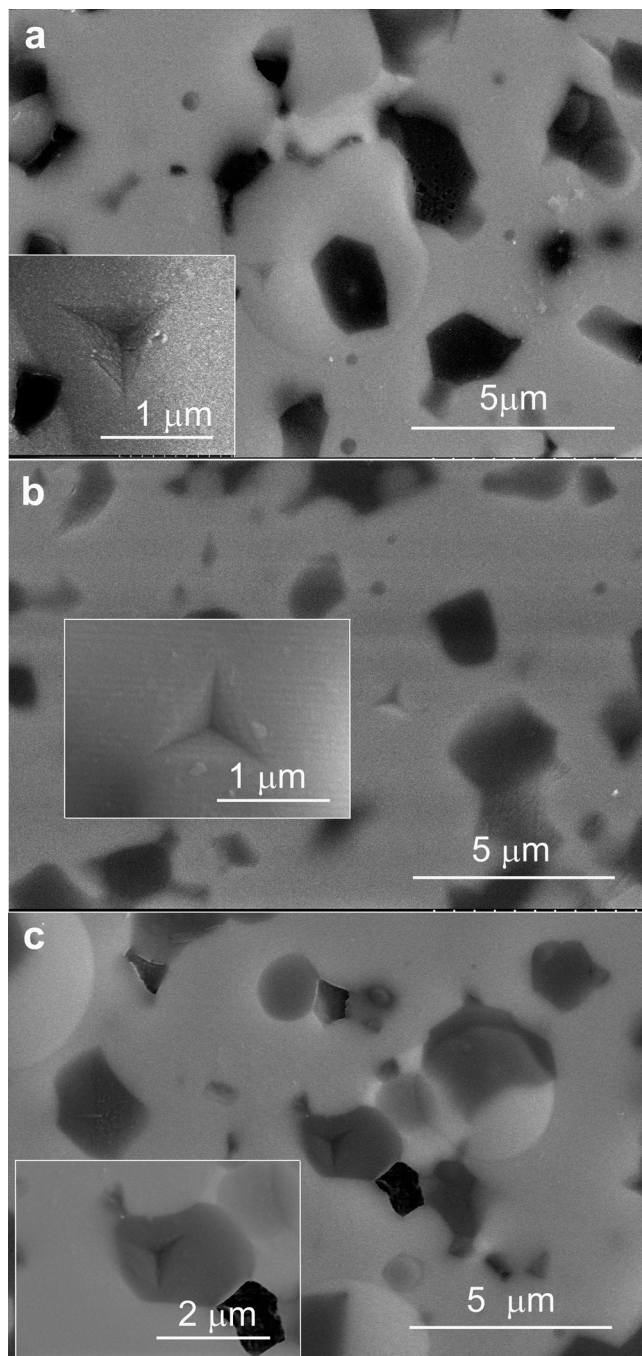

Fig. 4. Characteristic results from Berkovich nanoindentations (6 mN, 10 s). Residual imprints corresponding to the load versus depth curves used to determine the local properties of the different phases shown in Fig. 5. The imprints are totally embedded in the grains. FE-SEM micrographs.
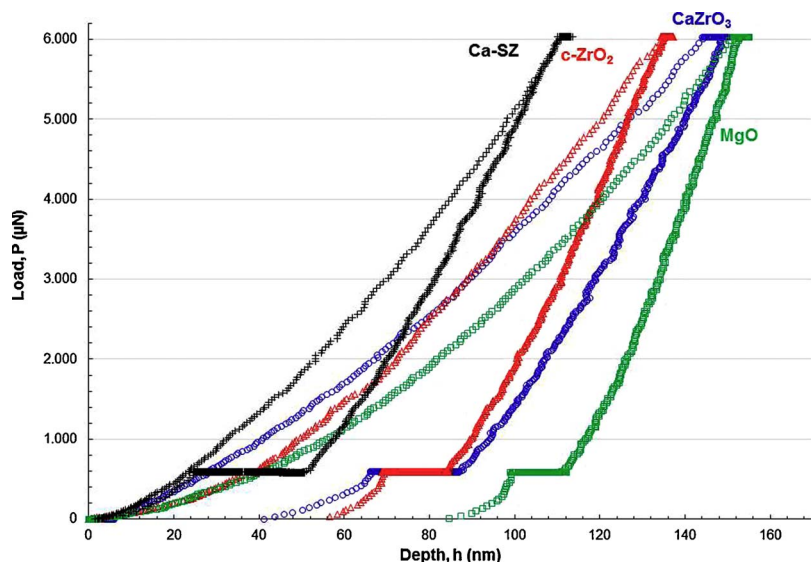a) c-ZrO$_2$.
b) CaZrO$_3$.
c) MgO.

Fig. 5. Characteristic results from Berkovich nanoindentations (6 mN, 10 s). Load versus depth curves used to determine the local properties of the different phases shown in Fig. 4 and the single phase Ca-stabilised ZrO₂ (Ca-SZ) bulk material. No discontinuities are observed.

indentations (Fig. 3b). Therefore, the values of the bulk properties for DNZ were highly variable, depending on the specific area tested. As a result, it is not possible to identify differences neither between Berkovich and Vickers hardness values for DNZ nor between Berkovich

hardness for DBZ and DNZ (Table 2).

The large cracks originated in polycrystalline samples during testing at relatively high loads, such as those observed in Figs. 2 and 3 do not affect the shape of the load-depth curves [41,45]. The presence of pop-in phenomena in the loading region of the load-depth curves is associated to occurrence non-elastic phenomena such as the elastic-plastic transition at low scale or phase transformation (e.g: [17]) in monocrystals and to fracture in the indenter-surface contact region in isotropic brittle materials such as soda-lime glass and fused silica [46]. The observed extensive microcracking and grain detachment under the indenter in DNZ can be responsible for the appearance of the "pop-in" event observed at the maximum load (Fig. 3c).

The characteristic imprints shown in Fig. 4 are small enough to be completely embedded in the grains and the associated P-h curves do not exhibit any sign of discontinuity that would reveal fracture-like phenomena. Thus, the obtained P-h can be used for extracting the mechanical properties of the individual phases, which retained their mechanical integrity throughout the indentation test.

The values of E and H calculated from the P-h curves plotted in Fig. 6 show clear distinct behaviours between the singular properties of the three main phases. Table 3 summarizes the average values of hardness and Young's modulus of the individual phases. For each phase, differences between the values obtained for the two materials are within the limits of the experimental variability.

The fact that values of the properties obtained for the individual phases are independent of the material (Table 3, Fig. 6) indicates that their contributions to the global behaviour of the materials are independent of their amount and the characteristics of the particles (size and shape).

Reported values for Young's modulus of MgO single crystals determined by nanoindentation summarised in Table 1 are similar to those determined in this work (Table 3). Hardness of the single crystal is coincident to our results for depths (h < 200 nm) similar to those
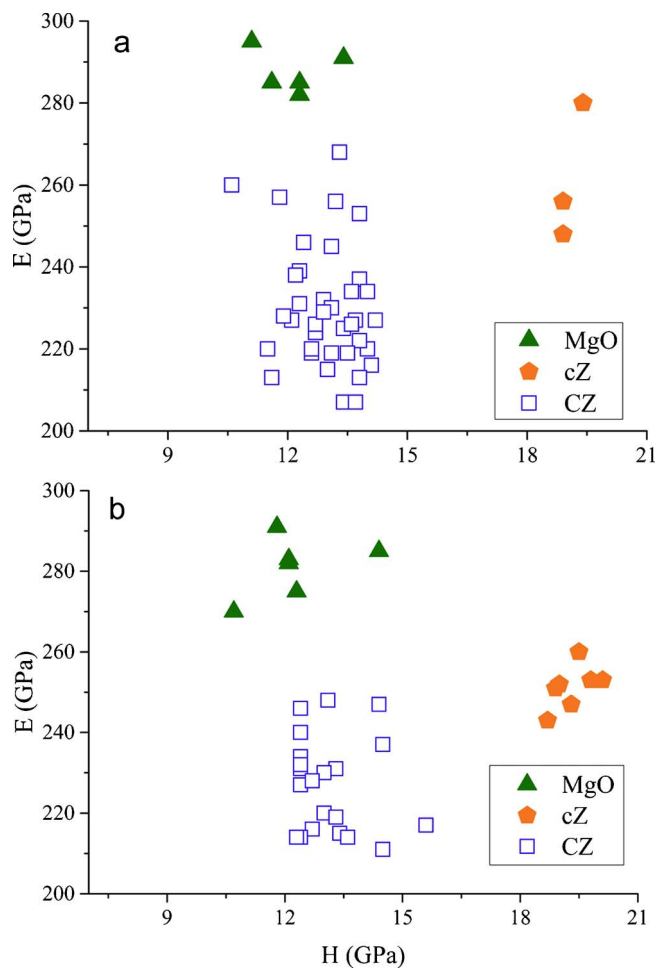

Fig. 6. Summary of calculated E and H values for all identified residual imprints indicating the corresponding phase.
a) Material DBZ.
b) Material DNZ.

Table 3
Hardness and Young modulus experimental values obtained for the individual phases.

Phase		H (GPa)	E (GPa)
DBZ	CaZrO₃	13.0 ± 0.8	230 ± 15
	MgO	12.1 ± 0.9	288 ± 5
	c-ZrO₂	19.1 ± 0.3	261 ± 16
DNZ	CaZrO₃	13.2 ± 0.9	227 ± 12
	MgO	11.9 ± 0.6	281 ± 7
	c-ZrO₂	19.3 ± 0.4	251 ± 5

Table 4
Values used to calculate bulk properties.

	Theoretical density (g/cm^3)	XRD file	Experimental		Literature		wt.%[***]		vol.%	
			E (GPa)	H (GPa)	E (GPa)	H (GPa)	DBZ	DNZ	DBZ	DNZ
CaZrO$_3$	4.61	01-076-2401	228 ± 17	13 ± 1			72.4	49.5	66.2	43.6
MgO	3.57	01-071-1176	284 ± 9	12 ± 1			18	14.7	21.3	16.7
c-ZrO$_2$	5.55	00-026-0341	256 ± 21	19.2 ± 0.5			2.1	15.3	1.6	11.2
Ca$_3$Mg(SiO$_4$)$_2$	3.34	00-035-0591			116 [51]	9.7 [50]	3.5	10.5	4.4	12.8
CMSZ glass	2.6	–			89[*]	7[**]	4	10	6.5	15.6

[*] Calculated for MgO-SiO$_2$-CaO glass according to [52], p. 376.

[**] SiO$_2$ glass [52], p. 413.

[***] Calculated from the contents of crystalline and non-diffracting phases determined by Rietveld.

used here (h < 150 nm, Fig. 5).

Results of Table 3 for c-ZrO$_2$ are similar to those obtained here for the industrial specimen of Ca-stabilised ZrO$_2$ and to those reported by Gaillard et al. [26] for single crystals and individual cubic grains of YSZ shown in Table 1.

Regarding MgO and c-ZrO$_2$, results for each phase are coincident in both materials. Moreover, there is a satisfactory agreement between the results listed in Table 3 for the grains of these phases in the studied composites and those for bulk ceramics of the same composition summarized in Table 1. Both facts sustain and validate the methodology implemented in this investigation for the extraction of the mechanical properties at the local (individual phase) level.

Up to the knowledge of the authors, this is the first time that nanoindentation values of H and E for CaZrO$_3$ are reported. There is a satisfactory agreement between the experimental results listed in Table 3 and those reported for bulk Young's modulus of dense CaZrO$_3$ ceramics (Table 1) while hardness values are higher ($\approx$18%) than values obtained using Vickers indentation in bulk materials.

Calculations following the Oliver-Pharr method assume a stiff and perfect conical indenter in contact with a plane. In reality, no Berkovich indenter is ideal and the point has spherical shape. The effect of this deviation from ideal is more significant in small indentations with respect to the tip radius, as the ones discussed in this work [47] and would lead to overestimated E and H values because the area included in calculations is smaller than the real one. However, calibration with a material of known properties help to overcome this effect and, in fact, Young's modulus values determined here for the grains of the different phases in the composites coincide with those of bulk ceramics, as discussed above.

Vickers hardness values for CaZrO$_3$ ceramics (Table 1) are significantly lower than those determined here by nanoindentation for the grains of this phase in the composites (Table 3). It is well known that hardness of material tends to increase with decreasing load; this scale effect is usually referred as indentation size effect (ISE) when it is due to plasticity. There have been identified other factors to this increase which depend on the specific material, especially in ceramics [48]. As discussed above for the composites, Vickers indentation values for CaZrO$_3$ ceramics could also be affected by microcracking due to residuals stresses originated in this phase with high thermal expansion anisotropy [42] what will lead to lower hardness values as compared to those of singular grains.

In order to analyze the contribution of the phases to the global behavior of the materials studied here, the values of hardness and Young's modulus of the two multiphase ceramics, DBZ and DNZ, were estimated using the superior limit of the "rule of mixtures" (Voight upper limit [49]). Values from Table 4 were used for calculations. The volumetric fractions of the phases were calculated from the weight fractions re-calculated taking into account the amount of glass and the theoretical densities. Hardness and Young's modulus of CaZrO$_3$, MgO and c-ZrO$_2$ were the averages and errors of the experimental values for the two materials. As it was not possible to determine the properties of

merwinite and glass, values were taken from the literature.

Regarding hardness, there is a fairly good agreement between the calculated values and those obtained using the large Berkovich indentation for material DBZ. For the larger Vickers indentations in both materials, values are significantly lower than those calculated from nanoindentation data, what would be explained by the scale effect discussed above. For both materials, the values of Young's modulus calculated using the Voight limit and the experimental bulk properties determined using the large Berkovich indentation are coincident.

5. Conclusion

It is possible to determine the Young's modulus, E, and the hardness, H, of the individual phases present in fine grained and dense CaZrO$_3$-MgO-ZrO$_2$ multiphase materials using nanoindentation tests, once the localisation of the imprints in the microstructure is assured by microscopical means. Properties of the individual phases are coincident to those of the corresponding single phase bulk materials. E and H of the individual phases are independent of the material; therefore their effective E and H in the composites are independent of their amount and the characteristics (size and shape).

The contribution of the individual phases to Young's modulus of the multiphase materials can be estimated from their Young's modulus using the Voight upper limit of the "rule of mixtures". Differences between hardness values estimated using this limit and those of microhardness tests are due to an indentation scale effect.

References

[1] C. Berger, H. Scheerer, J. Ellermeier, Modern materials for forming and cutting tools—overview, Materialwiss. Werkst. 41 (2010) 5–17.

[2] Z. Huda, P. Edi, Materials selection in design of structures and engines of supersonic aircrafts: a review, Mater. Des. 46 (2013) 552–560.

[3] D.R. Clarke, M. Oechsner, N.P. Padture, Thermal-barrier coatings for more efficient gas-turbine engines, Mater. Res. Soc. Bull. 37 (2012) 891–898.

[4] W.E. Lee, R.E. Moore, Evolution of in situ refractories in the 20th century, J. Am. Ceram. Soc. 81 (1998) 1385–1410.

[5] W.E. Lee, B.B. Argent, S.W. Zhang, Complex phase equilibria in refractories design and use, J. Am. Ceram. Soc. 85 (2002) 2911–2918.

[6] A.H. De Aza, P. Pena, J.E. Iglesias, S. De Aza, Ternary system Al$_2$O$_3$-MgO-CaO. Part II. Relationship in the subsystem Al$_2$O$_3$-MgAl$_2$O$_4$-CaAl$_4$O$_7$, J. Am. Ceram. Soc. 83 (2000) 919–927.

[7] P. Pena, B. Vázquez, A. Caballero, S. De Aza, Diagramas de equilibrio de fases cuaternarios. Métodos de representación e interpretación, Bol. Soc. Esp. Ceram. V 44 (2005) 113–122.

[8] S. Serena, M.A. Sainz, A. Caballero, Experimental determination and thermo-dynamic calculation of the ZrO$_2$-CaO-MgO system at 1600 1700, and 1750 °C, J.

Am. Ceram. Soc. 87 (2004) 2268–2274.

[9] S. Serena, M.A. Sainz, S. De Aza, A. Caballero, Thermodynamic assessment of the system ZrO$_2$-CaO-MgO using new experimental results: calculation of the isoplethal section MgO-CaO-ZrO$_2$, J. Eur. Ceram. Soc. 25 (2005) 681–693.

[10] F. Booth, L. Garrido, E. Aglietti, A. Silva, P. Pena, C. Baudín, CaZrO$_3$-MgO structural ceramics obtained by reaction sintering of dolomite-zirconia mixtures, J. Eur. Ceram. Soc. 36 (2016) 2611–2626.

[11] A. Silva, F. Booth, L. Garrido, E. Aglietti, P. Pena, C. Baudín, Sliding wear of CaZrO$_3$-MgO composites against ZrO$_2$ and steel, J. Eur. Ceram. Soc. 37 (2017) 297–303.

[12] A. Silva, F. Booth, L. Garrido, E. Aglietti, P. Pena, C. Baudín, Influence of phase composition on the sliding wear of composites in the system CaZrO$_3$-MgO-ZrO$_2$ against ZrO$_2$ and steel, Theor. Appl. Fract. Mech. 85 (Part A) (2016) 125–133.

[13] C. Hu, Z. Li, A review on the mechanical properties of cement-based materials measured by nanoindentation, Constr. Build. Mater. 90 (2015) 80–90.

[14] F.J. Ulm, M. Vandamme, C. Bobko, J.A. Ortega, Statistical indentation techniques for hydrated nanocomposites: concrete, bone, and shale, J. Am. Ceram. Soc. 90 (2007) 2677–2692.

[15] H.Y. Amanieu, D. Rosato, M. Sebastiani, F. Massimi, D.C. Lupascu, Mechanical property measurements of heterogeneous materials by selective nanoindentation: application to LiMn$_2$O$_4$ cathode, Mater. Sci. Eng. A—Struct. 593 (2014) 92–102.

[16] K.J. Krakowiak, P.B. Lourenço, F.J. Ulm, Multitechnique investigation of extruded clay brick microstructure, J. Am. Ceram. Soc. 94 (2011) 3012–3022.

[17] V.I. Kushch, S.N. Dub, R.S. Shmegera, Y.V. Sirota, G.N. Tolmacheva, Procedure of the multiple indentations for determination of the hardness parameters of structurally heterogeneous materials, J. Superhard Mater. 37 (2015) 173–181.

[18] I. Hussainova, E. Hamed, I. Jasiuk, Nanoindentation testing and modeling of chromium-carbide-based composites, Mech. Compos. Mater. 46 (2011) 667–678.

[19] W.C. Oliver, G.M. Pharr, Measurement of hardness and elastic modulus by instrumented indentation: advances in understanding and refinements to methodology, J. Mater. Res. 19 (2004) 3–20.

[20] G. Constantinides, K.S. Chandran, F.J. Ulm, K.J. Van Vliet, Grid indentation analysis of composite microstructure and mechanics: principles and validation, Mater. Sci. Eng. A 430 (2006) 189–202.

[21] C. Hu, Nanoindentation as a tool to measure and map mechanical properties of hardened cement pastes, MRS Commun. 5 (2015) 83–87.

[22] J.J. Chen, L. Sorelli, M. Vandamme, F.J. Ulm, G. Chanvillard, A coupled nanoindentation/SEM-EDS study on low water/cement ratio portland cement paste: evidence for C-S-H/Ca(OH)$_2$ nanocomposites, J. Am. Ceram. Soc. 93 (2010) 1484–1493.

[23] J. Mencik, D. Munz, E. Quandt, E.R. Weppelmann, M.V. Swain, Determination of elastic modulus of thin layers using nanoindentation, J. Mater. Res. 12 (1997) 2475–2484.

[24] J. Zhu, K.B. Yeap, K. Zeng, L. Lu, Nanomechanical characterization of sputtered RuO$_2$ thin film on silicon substrate for solid state electronic devices, Thin Solid Films 519 (2011) 1914–1922.

[25] C.A. Botero, E. Jiménez-Piqué, C. Baudín, N. Salán, L. Llanes, Nanoindentation of Al$_2$O$_3$/Al$_2$TiO$_5$ composites: small-scale mechanical properties of Al$_2$TiO$_5$ as reinforcement phase, J. Eur. Ceram. Soc. 32 (2012) 3723–3731.

[26] Y. Gaillard, M. Anglada, E. Jiménez-Piqué, Nanoindentation of yttria-doped zirconia: effect of crystallographic structure on deformation mechanisms, J. Mater. Res. 24 (2009) 719–727.

[27] J.J. Hughes, P. Trtik, Micro-mechanical properties of cement paste measured by depth-sensing nanoindentation: a preliminary correlation of physical properties with phase type, Mater. Charact. 53 (2004) 223–231.

[28] M. Dudek, G. Rog, W. Bogusz, A. Kozlowska-Rog, M. Bucko, L. Zych, Calcium zirconate as a solid electrolyte for electrochemical devices applied in metallurgy,

Mater. Sci.—Poland 24 (2006) 253–261.

[29] M. Dudek, E. Drozdz-Ciesla, Some observations on synthesis and electrolytic properties of nonstoichiometric calcium zirconate, J. Alloys Compd. 475 (2009) 846–854.

[30] D.W. Richerson, Modern Ceramic Engineering, Properties, Processing and Use in Design, 2nd ed. rev. and expanded., Publ. Marcel Dekker, Inc, New York, 2017 1992150 (chapter 4, p.150).

[31] H. Yang, Y. Ohishi, K. Kurosaki, H. Muta, S. Yamanaka, Thermomechanical properties of calcium series perovskite-type oxides, J. Alloys Compd. 504 (2010) 201–204.

[32] T.I. Hou, W.M. Kriven, Mechanical properties and microstructure of Ca$_2$SiO$_4$–CaZrO$_3$ composites, J. Am. Ceram. Soc. 77 (1) (1994) 65–72.

[33] C. Aksel, P.D. Warren, F.L. Riley, Magnesia-spinel microcomposites, J. Eur. Ceram. Soc. 24 (2004) 3119–3128.

[34] K. Kurosaki, D. Setoyama, J. Matsunaga, S. Yamanaka, Nanoindentation tests for TiO$_2$ MgO, and YSZ single crystals, J. Alloys Compd. 386 (2005) 261–264.

[35] D.W. Stollberg, J.M. Hampikian, L. Riester, W.B. Carter, Nanoindentation measurements of combustion CVD Al$_2$O$_3$ and YSZ films, Mater. Sci. Eng. A—Struct. 359 (2003) 112–118.

[36] G. Feng, W.D. Nix, Indentation size effect in MgO, Scr. Mater. 51 (2004) 599–603.

[37] R. Maurya, A. Gupta, S. Omar, K. Balani, Effect of sintering on mechanical properties of ceria reinforced yttria stabilized zirconia, Ceram. Int. 42 (2016) 11393–11403.

[38] R.W. Rice, Porosity of Ceramics, Marcel Dekker, Inc., 1998 (p. 102).

[39] Y. Bao, L. Liu, Y. Zhou, Assessing the elastic parameters and energy-dissipation capacity of solid materials: a residual indent may tell all, Acta Mater. 53 (2005) 4857–4862.

[40] J. Hay, Introduction to instrumented indentation testing, Exp. Tech. (November/ December) (2009) 66–72.

[41] S. Bueno, C. Baudin, Instrumented Vickers microindentation of alumina-based materials, J. Mater. Res. 21 (2006) 161–173.

[42] M.D. Mathews, E.B. Mirza, A.C. Momin, High temperature X-ray diffractometric studies of CaZrO$_3$, SrZrO$_3$ and BaZrO$_3$, J. Mater. Sci. Lett. 10 (1991) 305–306.

[43] S.P. Terblanche, Thermal-expansion coefficients of yttria-stabilized cubic zirconias, J. Appl. Cryst. 22 (1989) 283–284.

[44] W.E. Lee, W.M. Rainforth, Refractory materials, Ceramic Microstructures: Property Control by Processing, Chapman & Hall, London, UK, 1994, pp. 470–488.

[45] R.F. Cook, G.M. Parr, Direct observation and analysis of indentation cracking in glasses and ceramics, J. Am. Ceram. Soc. 73 (4) (1990) 787–817.

[46] D.J. Morris, S.B. Myers, R.F. Cook, Sharp probes of varying acuity: instrumented indentation and fracture behavior, J. Mater. Res. 19 (2004) 165–175.

[47] A. Rico, M.A. Garrido, E. Otero, J. Rodríguez, Nanoindentación en materiales cerámicos: efecto de la carga y de la geometría del indentador, Bol. Soc. Esp. Ceram. V 46 (5) (2007) 253–258.

[48] X.J. Ren, R.M. Hooper, C. Griffiths, J.L. Henshall, Indentation size effect in ceramics: correlation with H/E, J. Mater. Sci. Lett. 22 (2003) 1105–1106.

[49] W. Voigt, Uber die Bezichungen zwischen den beiden Elastizitaskonstanen isotroper Korper, Wied. Ann. 38 (1889) 573–587.

[50] R.M. Iacobescu, A. Malfliet, L. Machiels, P.T. Jones, B. Blanpain, Y. Pontikes, Stabilisation and microstructural modification of stainless steel converter slag by addition of an alumina rich by-product, Waste Biomass Valor. 5 (2014) 343–353.

[51] J.L. Rodriguez, C. Baudín, P. Pena, Relationships between phase constitution and mechanical behaviour in MgO-CaZrO$_3$-calcium silicate materials, J. Eur. Ceram. Soc. 24 (2004) 669–679.

[52] J.M. Fernández Navarro, El vidrio, Consejo Superior de Investigaciones Cientificas, Madrid, Spain, 2003 p. 376, p. 413.